い．一方，オザグレルナトリウムは，発症5日以内の脳血栓症に対して静脈内投与した場合に運動麻痺の改善が認められており，ラクナ梗塞が適応症として使用されている[41]．

急性期治療EBMの問題点

ランダム化比較試験では，十分なインフォームドコンセントを得て，プロトコールを遵守して治療適応を判定し，標準化された治療法を実行し，治療経過を十分に観察することが重要である．しかし，急性期治療では，高いエビデンスを得るためのこれらの過程を困難にする要因が数多く存在する．救急医療の現場では，限られた時間と少ない医療スタッフという環境のなかで，高い水準のEBMを実践するためには相当な努力を要する．さまざまなバイアスにより，レベル1のEBMの研究も水準が下がり，EBMとしての価値を喪失する危険性をはらんでいる．また，症例を無作為化試験に登録する時点で，適応外の症例を登録したり，登録漏れがあったり，登録せずに線溶療法を行ってしまったり，インフォームドコンセントが得られず登録できないなどの脱落症例が生じる可能性がある．

脳梗塞急性期症例に対してMRI検査が可能な施設では，CT上適応ありとして割り付けられた場合に，DWIで広範囲の高信号域が検出された症例をプロトコールどおりに治療することには，担当医としては抵抗があるが，治療中止するとプロトコール違反となり，どちらにしても深刻な問題となる．

局所線溶療法が地域住民に知られている救急医療施設では，局所線溶療法の有効性が証明されていないので臨床研究が必要であるという患者への説明に矛盾が生じる可能性がある．局所線溶療法のよい適応と思われる症例の場合，対照群に割り付けられることに，担当医師は抵抗を感じるかもしれない．こうした状況を乗り越えてプロトコールどおりに実施しなければならないところに，急性期治療EBMの抱える課題がある．

日常診療では，経験のある医師に教育機関で指導・訓練された若い医師は，その後，自分の経験を積み，各分野の権威といわれる研究者の研究結果を聞き，文献的考察から知識を得て自分自身の臨床経験の裏づけとする．こうして積み重ねた経験と知識から患者に適した治療を選択し実践する．

実際の診療では，その多くが経験に基づくものであり，"experience-based medicine"といえる．経験が臨床では重要なことであることには変わりがないが，その経験に裏打ちされたことが時代とともに変わることもある．経験を裏づけるためのエビデンスが必要であり，エビデンスだけですべて解決できるわけではないが，エビデンスのない医療は受け入れられない時代に入っているといっても過言ではない．しかし，日常臨床でエビデンスを得るには時間と労力がかかり，それに見合うリスクが伴うことも事実である．すべての点でエビデンスを得ることは不可能に近いことかもしれないが，一つでも多くのことにエビデンスを得るよう努力することが，患者を治療するうえでおおいに役に立つことは明らかである．

（根本　繁）

文　献

1) Bendszus M, et al. Outcome after local intra-arterial fibrinolysis compared with the natural course of patients with a dense middle cerebral artery on early CT. Neuroradiology 1998; 40: 54-8.
2) Weber J, et al. Diffusion-weighted imaging in ischaemic stroke: A follow-up study. Neuroradiology 2000; 42: 184-91.
3) Karonen JO, et al. Combined diffusion and perfusion MRI with correlation to single-photon emission CT in acute ischemic stroke: Ischemic penumbra predicts infarct growth. Stroke 1999; 30: 1583-90.
4) Sorensen AG, et al. Hyperacute stroke: Evaluation with combined multisection diffusion-weighted and hemodynamically weighted echo-planar MR imaging. Radiology 1996; 199: 391-401.
5) Ueda T, et al. Evaluation of risk of hemorrhagic transformation in local intra-arterial thrombolysis in acute ischemic stroke by initial SPECT. Stroke 1994; 25: 298-303.
6) Klotz E, et al. Perfusion measurements of the brain: Using dynamic CT for the quantitative assessment of cerebral ischemia in acute stroke. Eur J Radiol 1999; 30: 170-84.
7) Fibrinolytic Therapy Trialists' (FTT) Collaborative Group. Indications for fibrinolytic therapy in suspected acute myocardial infarction: Collaborative overview of early mortality and major morbidity results from all randomised trials of more than 1000 patients. Lancet 1994; 343: 311-22.
8) Donnan GA, et al. Trials of streptokinase in severe acute ischemic stroke. Lancet: 1995; 345: 578-9.
9) Multicentre Acute Stroke Trial-Italy (MAST-I) Group. Randomized controlled trial of streptokinase, aspirin, and combination of both in treatment of acute ischaemic stroke. Lancet 1995; 346: 1509-14.

10) 大友英一ほか．脳血栓症におけるウロキナーゼの臨床的有用性について―Placeboを対照とした多施設二重盲検法による試験．臨床評価 1985；13：711-51.
11) Albers GW, et al. The Standard Treatment with Alteplase to Reverse Stroke (STARS) study. JAMA 2000; 283: 1145-50.
12) The National Institute of Neurological Disorders and Stroke rt-PA Stroke Study Group. Tissue plasminogen activator for acute ischemic stroke. N Engl J Med 1995; 333: 1581-7.
13) Clark WM, et al. Recombinant tissue-type plasminogen activator (Alteplase) for ischemic stroke 3 to 5 hours after symptom onset. The ATLANTIS Study: A randomized controlled trial. Alteplase Thrombolysis for Acute Noninterventional Therapy in Ischemic. JAMA 1999; 282: 2019-26.
14) Hacke W, et al. Intravenous thrombolysis with recombinant tissue plasminogen activator for acute hemispheric stroke: The European Cooperative Acute Stroke Study (ECASS). JAMA 1995; 274: 1017-25.
15) Hacke W, et al. Randomised double-blind placebo-controlled trial of thrombolytic therapy with intravenous alteplase in acute ischaemic stroke (ECASS II). Lancet 1998; 352: 1245-51.
16) Kwiatkowski TG, et al. Effects of tissue plasminogen activator for acute ischemic stroke at one year. National Institute of Neurological Disorders and Stroke Recombinant Tissue Plasminogen Activator Stroke Study Group. N Engl J Med 1999; 340: 1781-7.
17) The NINDS t-PA Stroke Study Group. Intracerebral hemorrhage after intravenous t-PA therapy for ischemic stroke. Stroke 1997; 28: 2109-18.
18) Fiorelli M, et al. Hemorrhagic transformation within 36 hours of a cerebral infarct: Relationships with early clinical deterioration and 3-month outcome in the European Cooperative Acute Stroke Study I (ECASS I) cohort. Stroke 1999; 30: 2280-4.
19) Katzan IL, et al. Use of tissue-type plasminogen activator for acute ischemic stroke: The Cleveland area experience. JAMA 2000; 283: 1151-8.
20) Reed SD. Treatment with tissue plasminogen activator and inpatient mortality rates for patients with ischemic stroke treated in community hospitals. Stroke 2001; 32: 1832-40.
21) Barnwell SL, et al. Safety and efficacy of delayed intraarterial urokinase therapy with mechanical clot disruption for thromboembolic stroke. Am J Neuroradiol 1994; 15: 1817-22.
22) del Zoppo GJ, et al. PROACT: A phase II randomized trial of recombinant pro-urokinase by direct arterial delivery in acute middle cerebral artery stroke. PROACT Investigators. Prolyse in Acute Cerebral Thromboembolism. Stroke 1998; 29: 1255-6.
23) Lewandowski CA, et al. Combined intravenous and intra-arterial r-TPA versus intra-arterial therapy of acute ischemic stroke: Emergency Management of Stroke (EMS) Bridging Trial. Stroke 1999; 30: 2598-605.
24) Adams HP, Jr. Guideline for thrombolytic therapy for acute stroke: A statement of guidelines for thrombolytic therapy for acute stroke: A supplement to the guideline for the management of patients with acute ischemic stroke. A statement for healthcare professionals from a Special Writing Group of the Stroke Council, American Heart Association. Stroke 1996; 27: 1711-8.
25) Zeumer H, et al. Local intra-arterial fibrinolytic therapy in patients with stroke: Urokinase versus recombinant tissue plasminogen activator (r-TPA). Neuroradiology 1993; 35: 159-62.
26) Larrue V, et al. Risk Factors for Severe Hemorrhagic Transformation in Ischemic Stroke Patients Treated With Recombinant Tissue Plasminogen Activator. A Secondary Analysis of the European-Australasian Acute Stroke Study (ECASS II) Stroke 2001; 32: 438-41.
27) von Kummer R, et al. Acute stroke: Usefulness of early CT findings before thrombolytic therapy. Radiology 1997; 205: 327-33.
28) Keris V, et al.Combined intraarterial/intravenous thrombolysis for acute ischemic stroke.Am J Neuroradiol 2001; 22: 352-8.
29) Frey JL, et al. Intrathrombus administration of tissue plasminogen activator in acute cerebrovascular occlusion. Angiology 1995; 46: 649-56.
30) Ouriel K, et al. Prourokinase versus urokinase for recanalization of peripheral occlusions, safety and efficacy: The PURPOSE trial. J Vasc Interv Radiol 1999; 10: 1083-91.
31) Furlan A, et al. Intra-arterial prourokinase for acute ischemic stroke. The PROACT II study: A randomized controlled trial. Prolyse in Acute Cerebral Thromboembolism. JAMA 1999; 282: 2003-11.
32) Kase CS, et al. Cerebral hemorrhage after intra-arterial thrombolysis for ischemic stroke: The PROACT II trial. Neurology 2001; 57: 1603-10.
33) Theron J, et al. Local intraarterial thrombolysis in the carotid territory. Intervent Neuroradiol 1996; 2: 111-26.
34) Jensen O, et al. Thrombolytic therapy in acute occlusion of the intracranial internal carotid artery bifurcation. AJNR Am J Neuroradiol 1995; 16: 1977-86.
35) 小川 彰ほか．平成13年度厚生科学研究費補助金21世紀型医療開拓推進事業研究報告書．超急性期脳梗塞に対する局所線溶療法の効果に関する臨床研究．2002年4月．
36) International Stroke Trial Collaborative Group. The International Stroke Trial (IST): A randomised trial of aspirin, subcutaneous heparin, both, or neither among 19435 patients with acute ischaemic stroke. Lancet 1997; 349: 1569-81.
37) Saxena R, et al. Risk of early death and recurrent stroke and effect of heparin in 3169 patients with acute ischemic stroke and atrial fibrillation in the International Stroke Trial. Stroke 2001; 32: 2333-7.
38) 田崎義昭ほか．脳血栓症急性期に対する抗トロンビン薬MD-805の臨床的有用性―プラセボを対照とした多施設二重盲検群間比較試験．医学のあゆみ 1992; 161: 887.
39) CAST (Chinese Acute Stroke Trial) Collaborative Group. CAST: Randomised placebo-controlled trial of early aspirin use in 20,000 patients with acute ischaemic stroke. Lancet. 1997; 349: 1641-9.
40) ZhengMing Chen, et al. On behalf of the CAST and IST collaborative groups Indications for Early Aspirin Use in Acute Ischemic Stroke A Combined Analysis of 40 000 Randomized Patients From the Chinese Acute Stroke Trial and the International Stroke Trial. Stroke 2000; 31: 1240.
41) 大友英一ほか．脳血栓症急性期におけるOKY-046の臨床的有用性―プラセボを対象とした多施設二重盲検試験．臨床医薬 1991; 7: 353-88.

大規模試験の遂行に行政の壁

小川 彰 氏
岩手医大脳神経外科教授

EBMの普及に伴い、日本人におけるエビデンスの不足が指摘されている。われわれ研究者は、臨床試験の推進に努めているが、その実施に当たっては行政上の数々の制約が足かせになっている。

3者3様の行政見解に困惑

例えば、私が主任研究者を務める多施設共同ランダム化比較試験の一つに、「MELT（MCA-Embolism Local Fibrinolytic Intervention Trial）-Japan」がある。これは厚生科学研究費による研究で、入院受療、QOLを低下させる疾患として最も多い脳梗塞を対象としている。急性期脳梗塞患者を局所線溶療法群と対照群に割り付け、同療法の有効性を検証しようとするものだ。

研究班は当初、局所線溶療法には血栓溶解薬のt-PAを使いたいと厚生労働省に申し出た。だが、同省保険局の回答は、「保険適応外の薬剤を使うのであれば、混合診療になる。入院費すべてを研究費として各施設に負担してもらう」というものだった。そんな余裕があるはずもなく、結局、保険診療の枠内でウロキナーゼを使うことになった。

ところが、その後、同省医政局からは、「なぜ今さらウロキナーゼを用いた試験など行うのか。新たな治療薬であるt-PAを使って試験されたい」という趣旨の公式文書を受け取った。そこで今度は同省の医薬局（現在は医薬・食品局）に出向いたところ、「現在、t-PAは脳への適応拡大の治験を行っている最中。そのため、他の用途では使わないでほしい」と言われた。こうした3者3様の意見に振り回されながら、私は何度となく厚労省内をかけずり回った。

このような理由で、わが国の大規模臨床試験は多くの場合、保険診療の枠内で行わざるを得ないのが現状だ。新薬の治験とは異なり、患者さんにはそれ相応の金銭的負担もかかる。患者さんにとって、臨床研究の対象になることに何のメリットもない。また、現場の医師はインフォームド・コンセントを取り、患者さんやご家族の納得を得るのに多大な労力を使っている。要は、現場の医師の熱意と、患者さんと医師の信頼関係だけを頼りに試験を行っているのが実情だ。症例数が集まらず大規模臨床研究が進まないない理由の一つはここにある。

MELT-Japanの場合、当初、症例を3年間で200例集める予定だったが、実際には50数例（2003年末）にとどまっている。

硬直的な研究費の使用目的

臨床試験では、患者に有害事象が生じた場合の補償も欠かせないが、この損害保険料の支払いについても矛盾がある。民間保険会社には年度初めに保険料を支払わなければならないが、国からの研究費が支払われるのは年度末であり、事実上、施設側が立て替え払いをせざるを得ない。

前年度分の研究費で翌年度4月に保険料を支払おうとしても、年度ごとに研究評価が行われるため、次年度分の支出はできない。立て替えをするにしても、研究の継続が決定した後になる。「研究費を保険料に充ててもよい」と厚労省はいうが、実質的には支払えないのである。

行政の柔軟な対応を求む

国際的に認められる大規模研究が少ないからといって、日本の医学研究レベルが欧米に比べて遅れているというわけでは決してない。米国の学会からの評価も高く、日本の研究者が発案した試験基準を用いて海外で大規模試験が行われていたりもする。しかし、わが国では少人数での試験にとどまっており、国際的に認められる結果が出されていないことが残念でならない。

そもそも米国とは、医学研究に費やされる予算が20～30倍も違う。国の財政難は重々承知しているが、厚労省は、日本人におけるエビデンスの蓄積を推進する以上、せめて縦割り行政の弊害を取り除くなど体制を見直し、われわれの研究を支援してもらいたいと切に願っている。（談）

特集

血栓溶解療法のUp To Date

MELT Japanのその後

井上敬，小笠原邦昭
INOUE Takashi, OGASAWARA Kuniaki
岩手医科大学脳神経外科

MCA-Embolism Local Fibrinolytic Intervention Trial Japan：MELT Japanはウロキナーゼを用い急性期局所線溶療法の有効性を評価することを目的に平成13年度より開始された．現在登録症例は48例（2003年11月10日現在）であるが，2群間で有意差は得られていない．本研究では同時にCT撮像法および読影法の標準化をおこなった．その結果，初期虚血変化判定能が有意に向上したことが読影実験で確認された．今後は画像診断が適応基準に入っている研究では，標準化は必須の手段となる可能性が考えられた．

Key Words
CT，MELT，中大脳動脈閉塞，標準化

はじめに

脳梗塞急性期にt-PA静脈投与をおこなうことにより，患者転帰が改善することが大規模ランダム化比較試験にて示されている．しかしいまだわが国では認可が下りていない．また局所投与が静脈投与にくらべその効果にすぐれているか否かは検討されていない．

超急性期局所線溶療法多施設共同試験（MCA-Embolism Local Fibrinolytic Intervention Trial Japan：MELT Japan）はウロキナーゼを用い，急性期局所線溶療法の有効性を評価することを目的に平成13年度より開始された．

1 研究概要

MELT Japanは実際の症例登録は平成14年1月より開始された．対象は急性中大脳動脈閉塞による虚血性脳血管障害患者とした．選択基準は，1)血管撮影で急性中大脳動脈閉塞が確認された患者，2)発症時刻が特定可能で発症後6時間以内に局所線溶療法が開始できる患者，3)入院直後のCTでまったく変化を認めないか，病側に軽微な初期虚血変化のみを認めるもの，4)CT撮像後より2時間以内に局所線溶療法を開始できる患者，5)年齢20歳以上75歳以下，の5項目を満たすこととした．局所線溶療法群はウロキナーゼ動注をおこない，対照群は局所線溶療法（動注，静注どちらも）以外の一般的治療をおこなうこととした．エンドポイントは発症3ヵ月でのmodified Rankin Scale（0-2）を予後良好群とした．

本研究の特徴は，1)インターネット上での割り付けによる超急性期治療に対するランダム化試験であること，2)CT撮像法の標準化をおこなったこと，3)CT読影法の標準化をおこなったことである．

1．インターネット上での割り付け

MELT Japanでは対象症例が発症から6時間以内に治療開始できる症例に限定されている．そのために，大学医療情報ネットワーク（UMIN）の協力のもと，暗号通信システムによるインターネットを用いた割り付けがおこなわれた．研究者は事前に登録し，独自のIDおよびパスワードが付与され，これを用いることにより，24時間症例の登録，割り付けが可能となった（http://melt.umin.ac.jp/）．実際の登録方法は，血管撮影以外の選択基準を満たし，除外基準のいずれにも該当しない対象候補患者があった場合ただちに患者のイニシャルと生年月日をもってpre-registrationをおこなう．つづいて血管撮影をおこない，血管撮影の条件に合致し，インフォームドコンセントが得られた時点で，registrationをおこない，治療群の割り付けを得る．治療群の割り付けは，対象例を無作為にNIHSS，年齢，施設に関して最小化法で2群の平衡をとりながらおこなう．割り付けられた治療をただちにおこなう．

このような流れに沿って，これまで重大な問題点なく運用されている．ただし，脳血管撮影室にインターネットアクセス可能なコンピュータがなく，医局などの別室から実際に療法をおこなっている医師に電話で連絡を取りつつ，割り付けをおこなったなどの報告があった．本研究のようにリアルタイムで症例の登録，割り付けをおこなう必要がある疾患の場合，セキュリティーの問題さえクリアすれば，インターネットを用いる手法は有効であることが確認された．

2．CT撮像法の標準化

MELT Japanでは画像による適応症例の判断に，CTのみを用いた．これに関しては，研究開始当初さまざまな意見が存在した．MRI拡散強調画像，SPECTなどによる脳血流画像の必要性も考慮されたが，最終的に，装置が普及していること，24時間使用可能なこと，発症から6時間以内に治療を開始しなくてはならないことからCTのみを必須の検査とするに至った．ただし，初期虚血変化を鋭敏に描出するために特化した条件での撮像を義務づけた．CTでの適応基準はCTでまったく変化を認めないか，病側に軽微な初期虚血変化（島皮質，前頭・側頭弁蓋部に限局する吸収値のわずかな低下やシルビウス裂の消失，レンズ核の不鮮明化）のみを認めるもの，ただしCT撮影後より2時間以内に局所線溶療法を開始できる患者とした．

CT撮像条件を表❶に示す．ヘリカルスキャンを不可としたが，これはヘリカルスキャンでは初期虚血変化を判定するに十分な信号雑音比を得るのが困難だからである．実際の条件としては250mA，2秒スキャン以上の条件にて，比較的良好な信号雑音比が得られた．

各施設には上記条件にて実際に撮像したフィルムを画像判定中央委員会に送付してもらい，十分な画像が得られているか否かを症例登録に先立って検討した．

表❶　術前判定基準における初期虚血変化の判定

1) スキャン方式は装置の世代に関わらずコンベンショナルスキャンとする（ヘリカルスキャンは不可）．
2) スライス厚は原則としてテント上は8-10mm厚とする．
3) 再構成関数（フィルタ）は最適のものを選択する（頭部用に特に用意されていない場合はstandardで可）．
4) CRT上での観察，フイルムへの焼き付けは十分狭いWindow幅で行う（Window幅80以下を推奨）．
5) 管電圧，管電流，回転速度はメーカ，機種によって状況が大きく異なるので，推奨条件の設定は行わなかったがただし，回転速度（スキャン時間）は最新機種であっても180度/秒以下（2秒/回転以上）が望ましいとした．一般に管電圧，管電流は高いほど，回転速度は遅いほどコントラスト分解能は高くなり同時に患者被曝，X線管球の発熱/負荷も増大することをふまえ，各装置ごとに最適の条件で撮像するよう心がけるものとした．

（MELT Japanウェブページ（https://endai.umin.ac.jp/islet/melt/ct/ct_gl01.htm）より許可を得て転載）

表❷ 術前判定基準における初期虚血変化の判定

1) CTでまったく変化を認めない	→ 治療適応
2) シルビウス裂に限局する軽微な虚血変化 (島皮質、前頭側頭弁蓋部に限局する吸収値のわずかな低下やシルビウス裂の消失あるいは／かつレンズ核の不鮮明化)	→ 治療適応
3) シルビウス裂以外の皮質領域の脳溝の消失や淡い低吸収域	→ 治療非適応

(MELT Japanウェブページ（https://endai.umin.ac.jp/islet/melt/ct/ct_gl01.htm）より許可を得て転載)

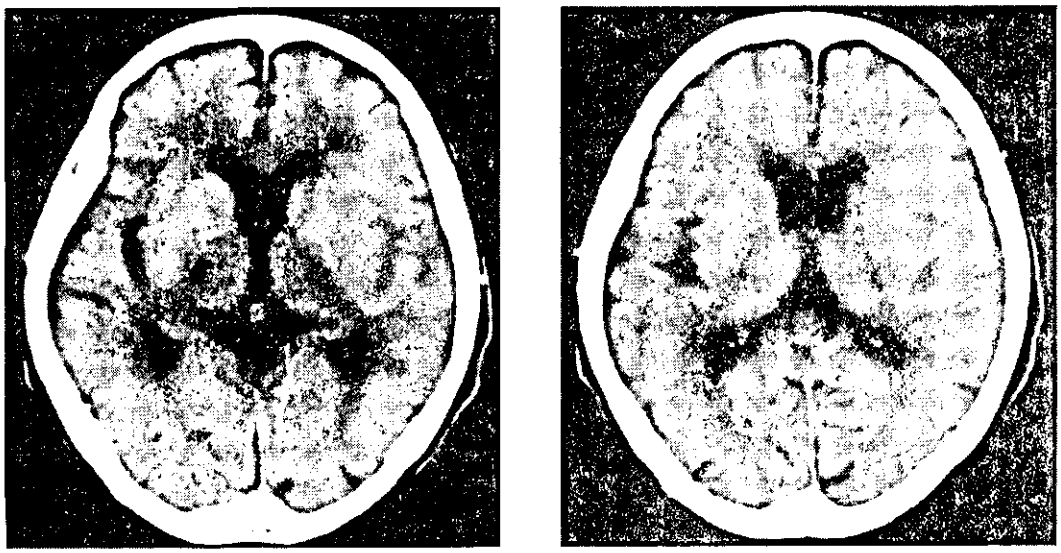

図❶ CTによる適応基準（初期虚血変化の範囲）
初期虚血変化が緑の領域のみに限定している場合は，治療適応あり．赤の領域に及んでいる場合は，治療非適応とした．(MELT Japanウェブページ（https://endai.umin.ac.jp/islet/melt/ct/ct_gl01.htm）より許可を得て転載)

3．CT読影法の標準化

CTにおける初期虚血変化の判定は決して平易ではなく，判定医は判定規準を十分に理解するとともに，所見判定に十分習熟している必要がある．判定の誤りは重大なプロトコール違反に直結し，本試験の質の低下につながる，との認識のもと，読影法の標準化をおこなった．また，インターネット上で実際の症例を用いた読影練習ができるシステムも構築し（https://endai.umin.ac.jp/islet/melt/ct/ct_gl01.htm），登録者であればいつでも練習可能なようにした．CTによる適応基準を表❷および図❶に示す．

4．CT撮像法および読影法標準化の効果

上記のとおり，MELT JapanではCT撮像法および読影法の標準化をおこない，適応基準を厳しく評価した．

また本研究では，標準化により局所線溶療法適応決定にかかわる診断能が向上するか否かを検討するために読影実験をおこなった．発症4時間以内の急性期脳塞栓症症例のCT画像を50部用意し，これを10名の放射線科医，脳神経外科医，神経内科医が2組に分かれて読影した．第一組は簡単なガイダンス後にすぐに読影をおこなった．第2組はガイダンスに加え上記標準化にもとづいた所見判定訓練プログラムを実施し，その後に読影をおこなった．その結果をreceiver operating characteristics（ROC）解析した．その結果，撮像法標準化のみおよび読影法標準化のみではどちらも局所線溶療法適応判定能は向上する傾向はみられたが，有意差は認めなかった．しかし両者を併用した場合に，非標準化群にくらべ有意に判定能が向上した（図❷）

2 中間解析

2003年11月10日現在で登録症例は48例である．これは目標症例の200例の半分以下にとどまっており，非常

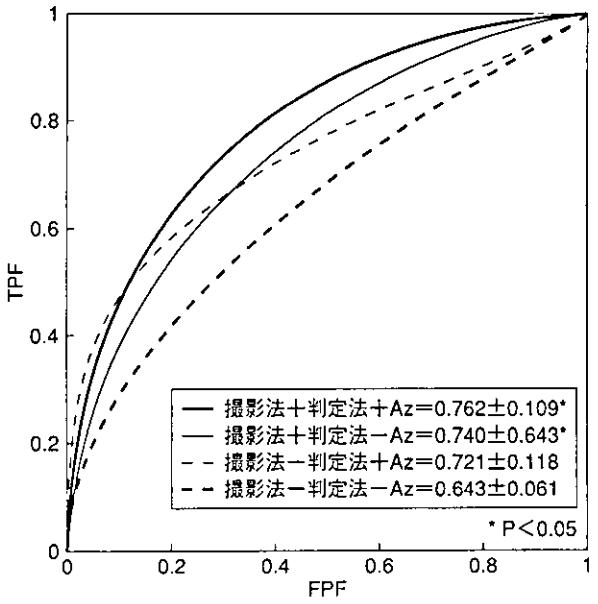

図❷ 標準化による局所線溶療法判定能
撮像法，読影法ともに非標準化の場合（太波線 ---）にくらべ，両者を標準化した群（太実線 ——）では有意に判定能が向上した．

に厳しい現状である．2003年9月に参加施設を対象に過去2年間の脳塞栓症症例をリストアップしたが，その結果予想以上に高齢者が多く，年齢による条件を満たさず，適応外とされた症例が多数みられた．また，発症数時間で来院した症例においても，本研究のCT撮像条件，読影法を使用した場合適応外となる初期虚血変化がみられることもわかった．症例数が予想をはるかに下回っている理由は上記2点が考えられる．

現時点で，割り付けは治療群，対照群で均等に割り付けられている．治療群において良好な臨床転帰が得られている症例が多く報告されているが，全体の症例数が少ないため有意差は得られていない．

プロトコール違反は数例あり，ほとんどはCT画像にて治療適応外の領域に初期虚血変化がみられているにもかかわらず，登録された症例であった．

おわりに

MELT Japanを通して，CT画像標準化の重要性が明らかになった．現在国内に広く普及しているCTであるが，撮像条件により初期虚血変化を鋭敏にとらえることができることは，意外に理解されていないと思われる．もちろんMRI拡散強調画像などの有用性を否定するものではないが，できるかぎりすみやかに治療を開始しなくてはならない中大脳動脈閉塞症のような疾患の場合，CTのみで適応を決定することは重要と思われる．また，撮像法の標準化をおこなうことはこれまでの研究ではほとんどおこなわれてこなかった．今回の研究を通して，日本国内においてさえ，またCT画像でさえ，標準化をおこなわなければ施設間での画質の差が研究結果に影響するほどの差異であることが確認された．今後は画像診断が適応基準に入っている研究では，標準化は必須の手段となる可能性が考えられた．

研究期間は残すところ数ヵ月となっているが，可能なかぎり登録証例数を増やすべく，努力をつづけているところである．

MELT Japan Homepage URLはつぎのとおりである．

http://melt.umin.ac.jp/

いのうえ・たかし

井上　敬　岩手医科大学脳神経外科
1966年，大阪府生まれ．
1993年，東北大学医学部卒業．1999年，脳神経外科専門医．2000年，医学博士．同年，岩手医科大学脳神経外科および付属超高磁場MRI研究施設助手．専門は，脳卒中の外科治療，MRI画像診断，脳機能画像．研究テーマは，MRIによる脳神経外科術前術後診断，脳機能画像．趣味は，旅行，読書．

AJNR Am J Neuroradiol 25:63–68, January 2004

Technical Note

Computational Simulation of Therapeutic Parent Artery Occlusion to Treat Giant Vertebrobasilar Aneurysm

Tamer Hassan, Masayuki Ezura, Eugene V. Timofeev, Teiji Tominaga, Tsutomu Saito, Akira Takahashi, Kazuyoshi Takayama, and Takashi Yoshimoto

Summary: We applied computational fluid dynamics (CFD) analysis to assess 3D digital subtraction angiography findings in a patient with a giant vertebrobasilar aneurysm to simulate and compare the consequences of left and right vertebral artery occlusion. The balloon occlusion test suggested that occlusion of the right vertebral artery is the better way to treat this patient's aneurysm from the point of view of aneurysmal thrombosis and isolation from the circulation. The computer simulation supported this conclusion, at the same time indicating that from the point of view of pressure distribution on the wall of the aneurysm, the right vertebral occlusion may be also accompanied by an undesirable effect. A high-pressure area on the aneurysm wall in systole was revealed. This high pressure potentially could lead to subsequent aneurysmal growth, which indeed occurred, as was revealed by a follow-up examination 6 months later. This study is a good example of possible future applications of CFD in patients with cerebrovascular disease before therapeutic intervention.

Endovascular occlusion of vertebral arteries has been established as one of the treatment modalities for vertebrobasilar aneurysms (1–6). This approach is based on the fact that hemodynamics play a crucial role in the formation of aneurysms and that the changes in hemodynamic flow pattern (ie, in velocity, pressure, and shear stress distributions) may potentially enhance thrombosis within aneurysms, which is favorable for their treatment.

In the present work, computational fluid dynamics (CFD) analysis based on 3D digital subtraction angiography findings in a patient with giant vertebrobasilar aneurysm was applied to simulate and compare hemodynamic consequences of left and right vertebral artery occlusion before endovascular therapy.

Received January 31, 2003; accepted after revision March 6.

From the Department of Neuroendovascular Therapy (T.H., M.E., A.T.), Tohoku University Graduate School of Medicine, Shock Wave Research Center, Institute of Fluid Science (E.V.T., T.S., K.T.), Tohoku University, and Department of Neurosurgery (T.T., T.Y.), Tohoku University, Sendai, Japan; and Ioffe Physico-Technical Institute, Russian Academy of Sciences (E.V.T.), St. Petersburg, Russia.

Address correspondence to Dr. Tamer Hassan, Department of Neuroendovascular Therapy, Tohoku University Graduate School of Medicine, 1–1 Seiryo-machi, Aoba-ku, Sendai 980-8574, Japan.

Case Presentation

A 66-year-old man presented to our hospital complaining of recent headache, right hearing loss, dysarthria, right facial palsy, and history of left homonymous hemianopia (2 years earlier). Previous MR and angiographic studies disclosed a giant aneurysmal mass with flow void located in the perimesencephalic and cerebellopontine angle cisterns that progressively increased in size over the past 2 years of conservative follow-up and eventually exerted marked compression on the brain stem and cerebellum, as shown in Figure 1.

Three-dimensional rotational digital subtraction angiography clearly elucidated that the giant aneurysm involved the two vertebral arteries and the basilar artery junction, with maximal aneurysmal dilatation at the exit of the right vertebral artery into the basilar artery, as shown in Figure 1. Poor collateral flow of the bilateral posterior communicating arteries was also observed during conventional digital subtraction angiography study (not shown).

The geometry of this aneurysm was so complex that it was difficult to decide which vertebral artery occlusion was the best treatment for this patient. To choose the best strategy, it was decided to carry out a balloon occlusion test. In addition, the surface geometry of the aneurysm was extracted from angiographic data and used for computational simulation of either left or right vertebral artery occlusion with subsequent analysis of the hemodynamic patterns in both cases.

Balloon Occlusion Test and Embolization Procedures

Balloon occlusion test and embolization procedures were performed with neuroleptic anesthesia to allow clinical neurologic examination. The balloon microcatheter (Copernic; Balt, Montmercy, France) was introduced in either vertebral artery through a 6F introducing catheter. Contralateral vertebral artery and bilateral internal carotid artery angiography were performed during the balloon occlusion test with a 5F diagnostic catheter.

During the balloon occlusion test, contrast material washout times and patterns were compared for right and left vertebral occlusions. Right vertebral artery therapeutic occlusion was found to be better than the left vertebral artery, because in this case contrast material washout time and contrast material stasis in the aneurysm was longer, indicating lower blood velocity inside the aneurysm and, hence, better conditions for aneurysmal thrombosis.

The patient underwent permanent right vertebral occlusion on the same day after balloon occlusion test by detachable coils. Under systemic heparinization, the right vertebral artery was catheterized by a 6F introducing catheter, through which a microcatheter (Excelsior 14, Boston Scientific, Watertown, MA) and guidewire (GT 12; Terumo, Tokyo, Japan) were inserted. Heparin was administered for 1 day after the procedure and tapered off without reversal.

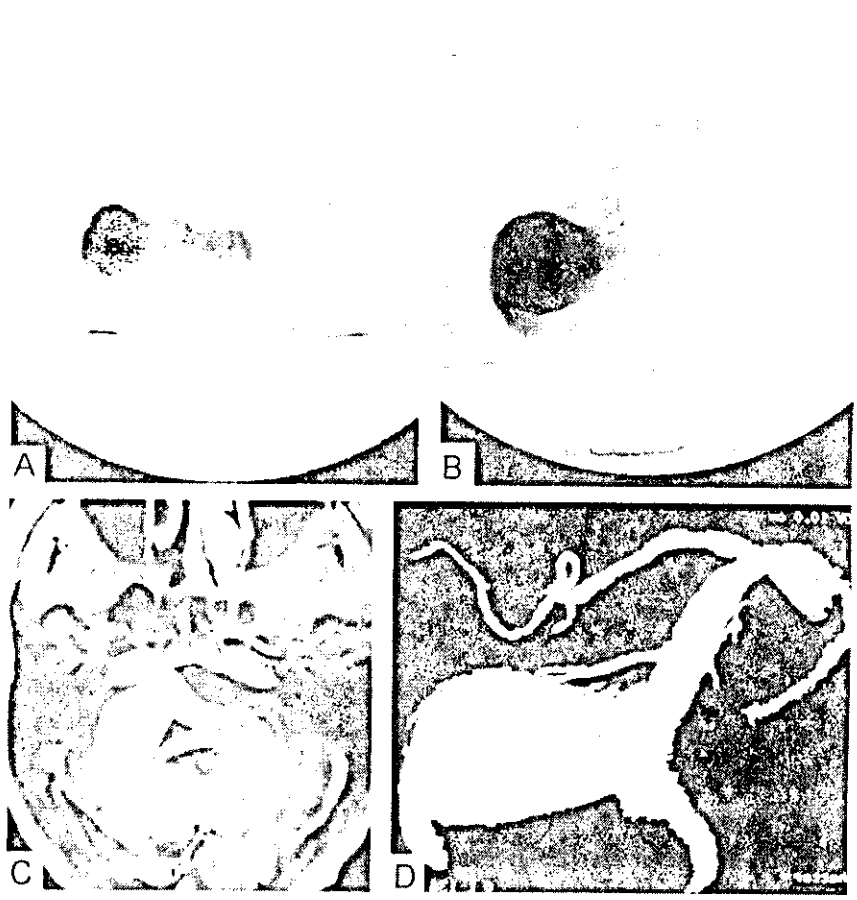

FIG 1. Pretreatment MR and angiographic images.

A, Left vertebral artery angiogram in the antroposterior view, arterial phase, on the patient's first clinical presentation 2 years ago shows the vertebrobasilar aneurysm and poor visualization of the basilar artery.

B, Recent follow-up of the left vertebral artery angiogram in the antroposterior view, arterial phase, shows progressive aneurysmal growth.

C, T1-weighted MR image with gadolinium injection demonstrates the aneurysmal mass effect in the posterior cranial fossa.

D, 3D digital subtraction angiogram with volume rendering through left vertebral injection shows giant aneurysm involving both vertebral arteries and basilar artery, with maximum dilatation over the right vertebral artery exit to basilar artery.

A cine MR imaging study was conducted before and after endovascular surgery, and the pattern of blood flow within the aneurysm was compared with the computer simulation results.

Computational Analysis

Rotational Angiography

An Advantx UNV system (GE Medical Systems, Milwaukee, WI) is used at our institution. A workstation (Advantage Workstation 3.1, GE Medical Systems) with data from rotational angiography was used to perform 3D digital subtraction angiography. Three-dimensional data sets were obtained from rotational series consisting of two rotations. The first one provided the subtraction mask. The C-arm was rotated 200° within 5 seconds at the exposure rate of 8.8 frames per second. A total of 44 images with matrix size of 512 × 512 pixels were acquired. The second rotation was performed during the administration of contrast material. Seventeen milliliters of contrast medium were automatically injected at a flow rate of 3 mL/s through a catheter positioned in the left vertebral artery by using a power injector (Medrad Mark V Plus; Sugan, Osaka, Japan). All 88 images of the mask data and contrast material data were immediately transferred to the Advantage Workstation for volume analysis via the network. A three-dimensional reconstruction algorithm based on the algebraic reconstruction technique was used to digitally produce 3D digital subtraction angiograms on the workstation within 8 minutes. Reconstructed images, including maximum intensity projection (MIP) and surface shaded display (SSD), and virtual endoscopic images were produced from the data. The algorithms used were MIP and SSD at an isosurface with mean threshold value of 1100 HU.

Cine MR Imaging

Cine MR imaging data were acquired by using cardiac gating to form a "movie" sequence of the blood flow pattern inside the aneurysm before and after therapeutic occlusion by using a 1.5-T MR imaging (Signa Horizon; GE Medical Systems) equipped with a standard head coil. After acquiring image in the sagittal plane (survey imaging), cardiac gated cine MR imaging (gradient echo sequence, 50/15/2 [TR/TE/NEX], flip angle, 45°; matrix, 256 × 192; and field of view, 24 cm) was then performed in the axial section, which crosses the aneurysm, and basilar artery (5 mm thickness). Imaging time was approximately 5–7 minutes.

Computational Flow Dynamics Modeling

The procedure of the extraction of surface geometry data from 3D digital subtraction angiograms and subsequent volume grid generation has been described in detail elsewhere (7, 8). The grid-generation software ICEM CFD, version 4.1 (ICEM CFD Engineering) was used to discretize the computational domain by using the boundary-fitted tetrahedral mesh containing 25,374 nodes and 123,838 tetrahedrons.

The governing equations are the three-dimensional incompressible unsteady Navier-Stokes equations written in strong conservative form for mass and momentum. They are discretized with a finite-volume method and solved in time-marching manner by using the pseudocompressibility technique. The simulation was performed with the following material constants: blood density, 1060 kg/m^3; blood dynamic viscosity, 0.004 Poiseuille (Pa.s). Blood was considered as a Newtonian fluid.

The software Fluent, version 6.0.12 (Fluent, Inc., Lebanon, NH) was applied to simulate physiologic pulsating flow in our

patient-specific computational model. The boundary conditions at open inflow boundaries (left and right vertebral arteries) were specified as the Fluent "velocity-inlet" boundary condition and were based on the pulsatile periodic flow rate obtained by Doppler ultrasonography (GE Medical Systems) of both vertebral arteries in the neck, which amounted to a mean velocity of 0.90 m/s. On the vessel walls, which were considered rigid, we applied the nonslip and nonpenetration conditions (ie, all velocity components at the vessel walls were set to zero—the "wall boundary" condition). The same condition was used to close ("occlude") inflow boundaries. For the outflow boundary (basilar artery), the Fluent "outflow boundary" condition was used. The simulation produced relative pressure values to be considered with respect to a basal pressure.

The simulation was initially performed for 3 seconds (over three cardiac cycles) with both vertebral arteries open. Then the occlusion of the left vertebral artery was modeled by applying the "wall-boundary" condition at the corresponding inflow boundary (the right vertebral artery remained open), and the computation was continued for another 3 seconds. Finally, the occlusion of the right vertebral artery was performed in the same manner ("wall boundary" condition at the inflow boundary of the right artery and "velocity-inlet" boundary condition at the inflow boundary of the left artery), followed by next 3 seconds of computation.

The SIMPLE method for solving the discretized equations was chosen. The unsteady flow was computed with a time step of 0.025 seconds. The time step was found to be sufficient from the point of view of accuracy. In the computational sequence described above, the results corresponding to the last (third) second of the cardiac cycle were considered to be independent from the initial conditions and used for flow analysis.

The simulation necessitated approximately 12 hours on a single processor of SGI Origin 2000 (Silicon Graphics, Inc, Mountain View, CA). To improve the convergence speed, relaxation factors were applied to velocity and pressure modifications. Flow visualization of Fluent's results was performed by means of the software Ensight, version 7.3.0 (Computational Engineering International, Inc., Berkley, CA). We also created a movie of the unsteady blood flow through the aneurysm before and after occlusion of either vertebral artery (one movie frame is shown in Figure 2).

Discussion

Several studies have been conducted to evaluate the hemodynamic effects of therapeutic vertebral artery occlusion to treat posterior circulation aneurysms, considering several model designs in a generalized approach (9–14). Cerebral arteries and, in particular, aneurysms are very different in shapes, sizes, and wall characteristics, making it difficult to judge their flow dynamic behavior and necessitating a "case-by-case" approach to each patient to determine the manner of treatment.

Vascular geometry appears to be an important factor in determining blood flow patterns. Computational flow simulation of every patient's vascular geometry may be a promising technique to reveal blood flow behavior, especially in geometrically difficult cases (7, 8, 14). Application of CFD to the case presented in this article, with poor bilateral cross posterior communicating artery flow, was especially useful because the posterior circulation was nearly isolated from the anterior one.

It is important to remember that any computer model is based on a number of assumptions. In the present study, for instance, blood is considered as a Newtonian fluid, and vessel and aneurysm walls as rigid. It seems safe to consider these assumptions to be of secondary importance in comparison with the influence of geometry and pulsating nature of blood flow, which are the most significant factors for prediction of possible aneurysmal growth. In fact, the entire strategy of treating patients with difficult giant vertebrobasilar aneurysms by unilateral vertebral artery occlusion (ie, by altering the geometry) is based on the assumption that this occlusion may change the local aneurysmal hemodynamics and, accordingly, enhances its thrombosis (1–3).

In addition to the model assumptions, another limitation of computational analysis is that it is not possible, with current computer resources and time limitations inherent to clinical practice, to evaluate the influence on the aneurysm hemodynamics of all model parameters (such as heart rate and rhythm, blood pressure, etc.) and their variations in time. Although computer modeling allows for easy manipulation with these parameters, at present we usually deal with just a few representative cases revealing only the most essential hemodynamic features of the aneurysm under study.

During the diagnostic angiography procedure, we observed that injection of contrast material through the left vertebral artery resulted in better visualization of the basilar artery than when contrast material was injected into the right vertebral artery, in which case the basilar artery was not visualized at all (not shown). Moreover, the results of the balloon occlusion test showed longer contrast material washout time and contrast material stasis in the aneurysm during right vertebral artery occlusion.

The above-mentioned angiographic findings were very useful in determining that occlusion of the right vertebral artery is more effective; however, they supplied us only with general blood flow patterns. Neither diagnostic angiography nor balloon occlusion test can give us any data regarding details of velocity distribution and its variation or other hemodynamic parameters, such as pressure (normal stress), shear stress, etc. Assisting computational simulation of vertebral occlusion may be needed to study each hemodynamic parameter in more detail and interpret them separately and in combination.

Our computer simulation results confirmed that right vertebral artery blood flow contributes more to the flow inside the aneurysm than does the flow coming from the left artery (Fig 2); however, the surface pressure map for the geometry under investigation after right vertebral artery occlusion showed significant pressure variations over the whole surface (of the order of 6 mm Hg in peak systole). In particular, a localized high-pressure spot was revealed on the aneurysm wall, right in front of the blood stream coming from the left vertebral artery. This finding led us to conjecture that future aneurysm re-growth may begin at this location. Six-month follow-up showed that this conjecture was correct: such re-growth has eventually occurred, as shown in Figure 3.

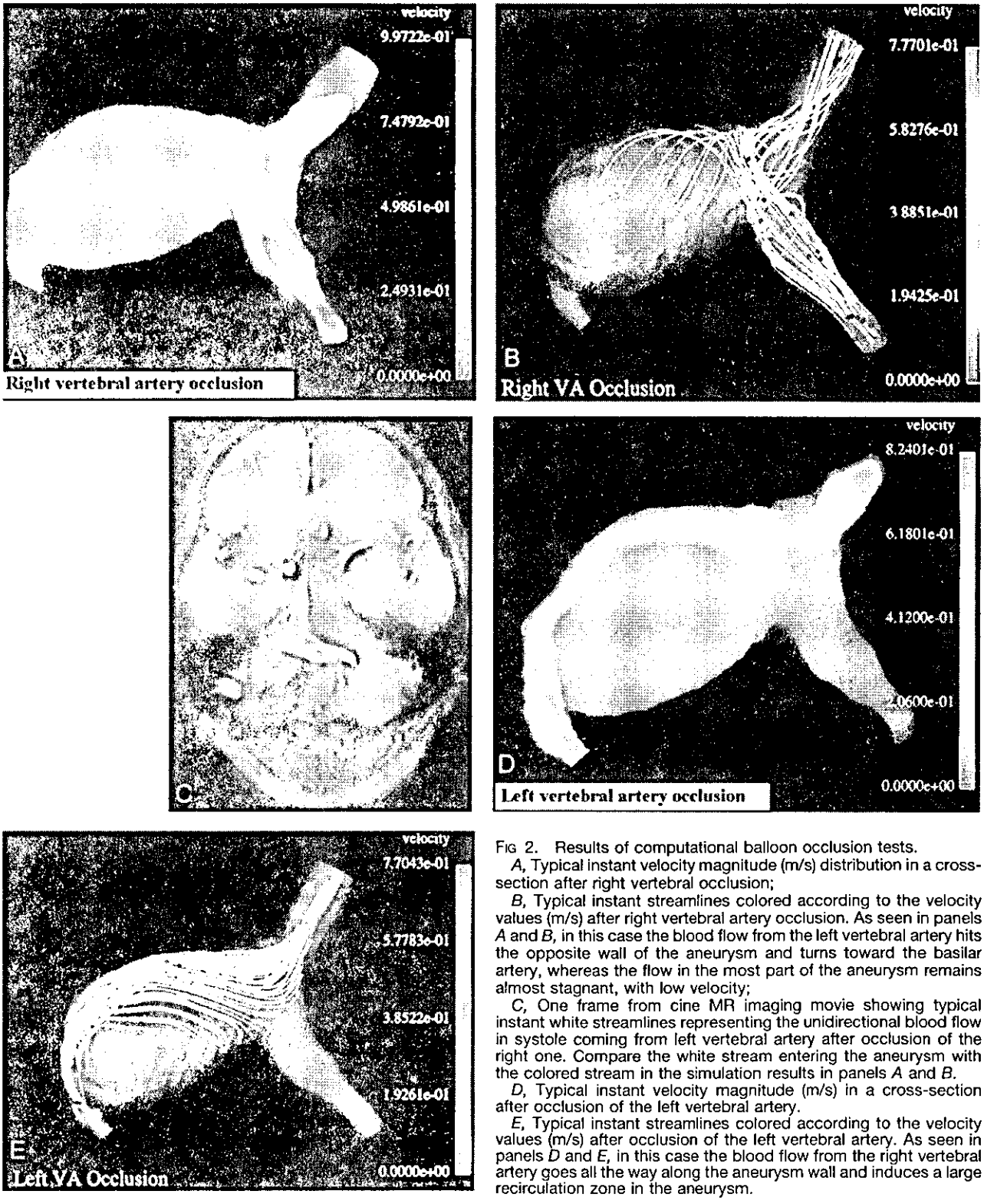

FIG 2. Results of computational balloon occlusion tests.

A, Typical instant velocity magnitude (m/s) distribution in a cross-section after right vertebral occlusion;

B, Typical instant streamlines colored according to the velocity values (m/s) after right vertebral artery occlusion. As seen in panels *A* and *B*, in this case the blood flow from the left vertebral artery hits the opposite wall of the aneurysm and turns toward the basilar artery, whereas the flow in the most part of the aneurysm remains almost stagnant, with low velocity;

C, One frame from cine MR imaging movie showing typical instant white streamlines representing the unidirectional blood flow in systole coming from left vertebral artery after occlusion of the right one. Compare the white stream entering the aneurysm with the colored stream in the simulation results in panels *A* and *B*.

D, Typical instant velocity magnitude (m/s) in a cross-section after occlusion of the left vertebral artery.

E, Typical instant streamlines colored according to the velocity values (m/s) after occlusion of the left vertebral artery. As seen in panels *D* and *E*, in this case the blood flow from the right vertebral artery goes all the way along the aneurysm wall and induces a large recirculation zone in the aneurysm.

Cine MR imaging was performed before and after therapeutic occlusion to compare the blood flow patterns and visually inspect how much of the aneurysm volume is eventually clotted after the occlusion. Preoperative cine MR imaging movie revealed vortex flow within the aneurysm (not shown); such vortex flow disappeared completely after therapeutic occlusion. Instead, postoperative unidirectional flow was observed in the left vertebral artery and adjacent area of the aneurysm, together with significant aneurysmal thrombosis (3 months after endovascular treatment). These findings were found to be in correspondence with our computational results, as shown in Figure 2.

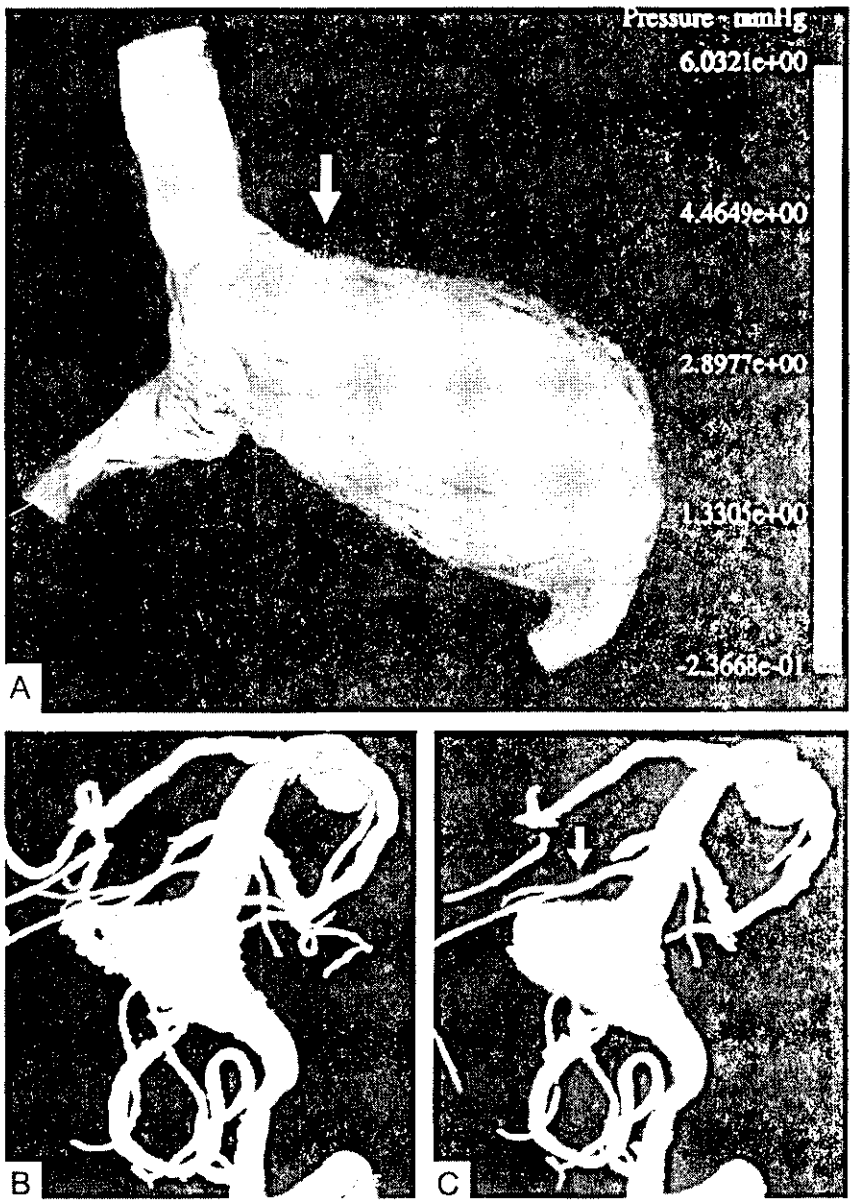

FIG 3. Comparison of the computational result for the right vertebral artery occlusion with follow-up angiograms.

A, Typical instant surface pressure (mm Hg) for the entire geometry after occlusion of the right vertebral artery, showing a higher pressure area (*white arrow*) on the wall opposite to the blood stream coming from the right vertebral artery. The locally higher normal stress may lead to subsequent growth of the aneurysm at this location.

B, 3D digital subtraction angiogram with volume rendering through left vertebral injection 3 months (*B*) and 6 months (*C*) after occlusion of the right vertebral artery. Note that the aneurysm started to grow again in the highest pressure area (*white arrow*) that was predicted computationally (see panel *A*).

Conclusion

Our computer simulation confirmed that right vertebral artery occlusion is the best available option for this patient. At the same time, the discovery of a higher pressure area after the occlusion, on the aneurysmal wall opposite to the blood stream coming from the left vertebral artery, indicated that this treatment might be ineffective for this patient in the long term because of possible future growth of the aneurysm. Such re-growth was indeed detected by the follow-up examination 6 months later. This case study provides an example of possible future applications of CFD in patients with cerebrovascular disease before therapeutic intervention.

References

1. Aymard A, Gobin P, Hodes JE, et al. **Endovascular occlusion of vertebral arteries in the treatment of unclippable vertebrobasilar aneurysms.** *J Neurosurg* 1991;74:393–398
2. Drake CG. **Ligation of vertebral arteries (unilateral or bilateral) or basilar artery in the treatment of large intracranial aneurysms.** *J Neurosurg* 1975;43:255–274
3. Hoh BL, Putman CM, Budzik RF, et al. **Combined surgical and endovascular techniques of flow alteration to treat fusiform and complex wide-necked intracranial aneurysms that are unsuitable for clipping or coil embolisation.** *J Neurosurg* 2001;95:24–35
4. Redkop G, TerBrugge K, Willinsky R. **Subarachnoid hemorrhage from vertebrobasilar dissecting aneurysm treated with staged bilateral vertebral artery occlusion: the importance of follow-up angiography: technical case report.** *Neurosurgery* 1999;45:1258–1263
5. Steinberg GK, Drake CG, Peerless SJ. **Deliberate basilar or vertebral artery occlusion in the treatment of intracranial aneurysms: immediate results and long-term outcome in 201 patients.** *J Neurosurg* 1993;79:161–173
6. Taki W, Nakahara I, Sakai N, et al. **Large and giant middle to lower basilar trunk aneurysms treated by surgical and interventional methods.** *Neurol Med Chir (Tokyo)* 1998;38:826–835
7. Hassan T, Saito T, Timofeev E, et al. **Numerical simulations of blood flow in cerebral vessels with aneurysms.** In: *Proceedings of the Fifth International JSME-KSME Fluids Engineering Conference.* Nagoya, Japan, November 17–21, 2002;235–240
8. Hassan T, Timofeev E, Ezura M, et al. **Hemodynamic analysis of an adult vein of Galen aneurysm malformation by use of 3D image-**

based computational fluid dynamics. *AJNR Am J Neuroradiol* 2003; 24:1075–1082
9. Kawanishi M, Nagasawa S, Ohta T, et al. **Simulation study on therapeutic vertebral artery occlusion for VA-PICA giant aneurysm.** *Neurol Res* 1994;16:100–103
10. Kerber CW, Knox HK, Buxton RB, Meltzer HS. **Flow dynamics in a fatal aneurysm of the basilar artery.** *AJNR Am J Neuroradiol* 1996;17:1417–1412
11. Nagayasu S. **Parent artery occlusion therapy for giant aneurysms of the vertebrobasilar system: hemodynamic analysis by hydraulic vascular model.** *Nippon Geka Hokan* 1992;61:156–167
12. Nagasawa S, Kawanishi M, Tada Y, et al. **Simulation of therapeutic parent artery occlusion for basilar head aneurysms: hemodynamic effect of occlusion sites and diameters of collateral arteries.** *Neurol Res* 1999;21:180–184
13. Tateshima S, Murayama Y, Villablanca P, et al. **Intraaneurysmal flow dynamics study featuring an acrylic aneurysm model manufactured using a computerized tomography angiogram as a mold.** *J Neurosurg* 2001;95:1020–1027
14. Foutrakis GN, Yonas H, Sclabassi RJ. **Finite element methods in the simulation and analysis of intracranial blood flow.** *Neurol Res* 1997;19:174–186

Computational Replicas: Anatomic Reconstructions of Cerebral Vessels as Volume Numerical Grids at Three-Dimensional Angiography

Tamer Hassan, Eugene V. Timofeev, Tsutomu Saito, Hiroaki Shimizu, Masayuki Ezura, Teiji Tominaga, Akira Takahashi, and Kazuyoshi Takayama

BACKGROUND AND PURPOSE: **We present a relatively simple approach that physicians can use to reconstruct cerebral vessels as 3D numerical grids or *computational replicas*. The method accurately duplicates their geometry to provide computer simulations of their blood flow.**

METHODS: **Initial images were obtained by using any medical imaging technique, such as MR angiography, CT angiography, or 3D digital subtraction angiography. The data were collected in DICOM format and converted by a DICOM reader into a 3D gray-scale raster image. The image was then processed by using commercial visualization and mesh generation software, which allowed extraction of the luminal surface of the blood vessel (by using the isosurfacing technique). The subsequent final output was an unstructured tetrahedral grid that can be directly used for detailed analysis of cerebral vascular geometry for patient-specific simulations of blood flow.**

RESULTS: **Four examples of grid reconstruction and blood flow simulation for patients with ruptured aneurysms were validated with angiographic and operative findings. The ruptured areas were correlated with areas of high fluid-induced wall-shear stress.**

CONCLUSION: **This approach promises to be a practical tool for planning treatment and follow-up of patients after neurosurgical or endovascular interventions with 3D angiography. The proposed commercial packages or conceptually similar ones seem to be relatively simple and suitable for direct use by neurosurgeons or neuroradiologists.**

The treatment of vascular diseases of the brain requires an understanding of hemodynamic factors that play an important role in their development. Numerous studies have been conducted to understand the initiation, progression, and rupture of intracranial aneurysms because of their fatal outcomes (1). Researchers have used tubes made of rigid glass (2, 3), acrylic (4), or silicon rubber (5, 6) for in vivo works in animal aneurysmal models (7) and human anatomic replicas of cerebral vessels imitating real aneurysmal geometries (5, 6). Simple aneurysmal geometries have been studied by using computational fluid dynamics (CFD) to understand the properties of blood flow around aneurysms (8–15).

Tremendous developments in computer hardware and software during the last decade have made it more feasible to create a user-oriented computational system to reveal the individual patterns of hemodynamic flow in patients with cerebrovascular diseases. These systems aim to display individual physiologic variations in a practical and time-efficient way and provide a bridge between medical professionals and flow dynamicists. The present study may be considered as a step toward this goal. It focused on detailed anatomic reconstructions of cerebral vessels with complex geometry to serve as accurate 3D grid models (computational replicas) for computer simulations of their blood flow.

Received October 6, 2003; accepted after revision January 15, 2004.

From the Departments of Neuroendovascular Therapy (T.H., M.E., A.T.) and Neurosurgery (T.T.), the Aerospace Research Laboratory (T.S.), Department of Mechanical System Engineering, Muroran, Japan, the Tohoku University Biomedical Engineering Research Organization (E.V.T., T.S., K.T.), Tohoku University, and the Department of Neurosurgery, Kohnan Hospital (H.S.), Sendai, Japan, and the Department of Mechanical Engineering, McGill University, Montreal, Canada (E.V.T.).

Supported by the Government of Japan as a part of the 21-Century Center of Excellence (COE) program.

Presented in part at the 19th Annual Meeting of the Japanese Society of Intravascular Neurosurgery, Yokohama, Japan, November 17, 2003.

Address reprint requests to Tamer Hassan, MD, Department of Neuroendovascular Therapy, Tohoku University Graduate School of Medicine, 2–1 Seiryo-machi, Aoba-ku, Sendai 980-8574, Japan.

The key element of such an image processing and computational system is the extraction of the vascular luminal surface from medical image data; the term *segmentation* is traditionally used for this procedure. The subsequent steps—volume mesh generation and flow modeling—are traditional and well-established procedures in CFD. A few approaches to segmentation are known from the literature. The initial stage in most of them is the performance of separate luminal segmentation for each 2D image or data section. At the next stage, once the series of lumen contours is obtained, the luminal surface is reconstructed by using splines (16), contour tiling (17) or other similar methods. The main disadvantage of this rather sophisticated approach is that it involves a great deal of manual, time-consuming work, especially in complex geometries with branching vessels (16). No integrated, commercially available software packages seem to offer such segmentation methods. In most cases, researchers use codes developed in-house or combinations of commercial codes, libraries, and in-house developments (8, 18, 19). Computer-aided drafting (CAD) systems, which are fairly difficult to learn and operate, are often involved (18, 19). Thus, it is not easy for clinicians to implement such methods and use them in their daily practice if they do not have substantial knowledge of computer graphics, computational mathematics, and related fields.

It is generally obvious that a direct 3D segmentation technique (without resorting to 2D contours) allows a higher degree of automation (20, 21). An interesting and time-efficient virtual balloon method (22) has been proposed; in it, a spherical balloon with a triangulated surface is inserted inside the lumen and then inflated to assume the shape of the lumen. At present, implementation of the technique requires its programming from scratch. It also remains to be seen how it would perform for really complex geometries; the example of a branching vessel given in reference 22 is fairly simple.

We sought to determine how 3D imaging data collected in DICOM format can be used to create numerical grids for computer simulations of blood flow in a relatively simple way that non-CFD specialists could perform after minimum training. To achieve this goal, we used well-established, commercially available software packages, particularly Advanced Visual Systems/Express software, to extract luminal vessel surfaces; this was done with the easy and automatic procedure of isosurfacing at an operator-specified gray-scale value. This approach also belongs to the direct 3D segmentation methods, which immediately result in a triangulated 3D luminal vascular surface.

Methods

The flowchart of patient-specific computational grid reconstruction and blood flow numerical simulation in Figure 1 indicates the main tools (numbered 1–6) of the procedure and the respective output formats (a–f). The whole process consists of five logical steps (I–V). In step I, primary medical images in DICOM format are obtained. In step II, they are transformed into a format suitable for the software that will be extracting

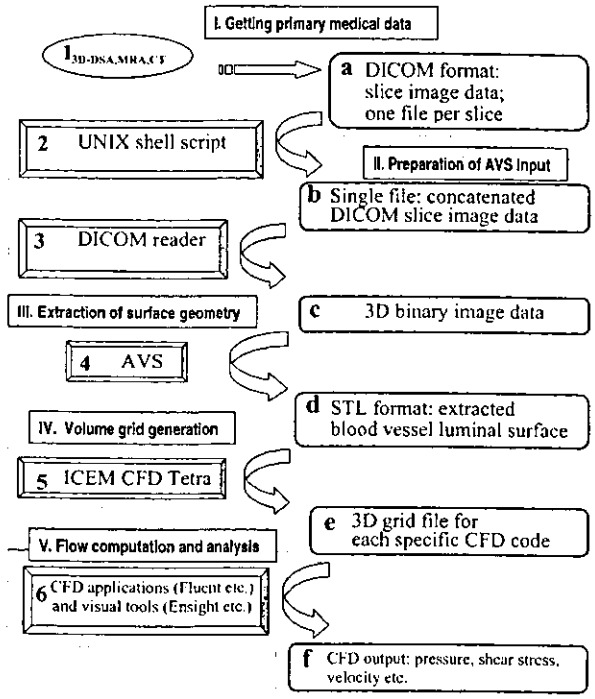

FIG 1. Flowchart of patient-specific segmentation, volume grid generation and blood flow analysis shows software tools (1–6) and output formats (a–f). I–V denote major stages of the procedure.

the luminal surface of the blood vessels of interest in step III. In step IV, the surface data are then imported by a grid generator, which creates a volume grid. The resulting grid model is used at step V for the numerical simulation of blood flow.

Rotational Digital Subtraction Angiography:

We obtained 3D datasets (Advantx UNV; GE Medical Systems, Milwaukee, WI) from rotational series consisting of two rotations. The first rotation provided the subtraction mask. The C-arm was rotated 200° in 5 seconds at the exposure rate of 8.8 frames per second. A total of 44 images with a matrix size of 512 × 512 pixels were acquired. The second rotation was performed simultaneously with the administration of contrast material. All 88 images were immediately transferred via our network to a workstation (Advantage Unix; GE Medical Systems) for volume analysis. A 3D reconstruction algorithm based on the algebraic reconstruction technique was used to digitally produce 3D digital subtraction angiography (DSA) images (Fig 2A and B) on the workstation within 8 minutes. Algorithms were maximum intensity projection (MIP) and surface-shaded display (SSD) at an isosurface with a mean threshold value of 1100 H.

The image displayed on the monitor was subjected to reformatting into transverse regularly spaced sections (Fig 2C). The batch function of the volume analysis allowed us to set up this set of sections rapidly. It was possible to preview the set as an animated sequence (movie loop) and save it on the image disk as sections in secondary DICOM format (Fig 2D). At the end of this stage, a separate data file for each section was generated. The file contained image data and other relevant information, such as the image size and patient's name.

Larger numbers of sections and decreased spaces between them improved the final mesh quality. In our experience, the number of sections for 3D DSA should be in the range of 300–700 sections, with a 0.1–0.2-mm distance between the

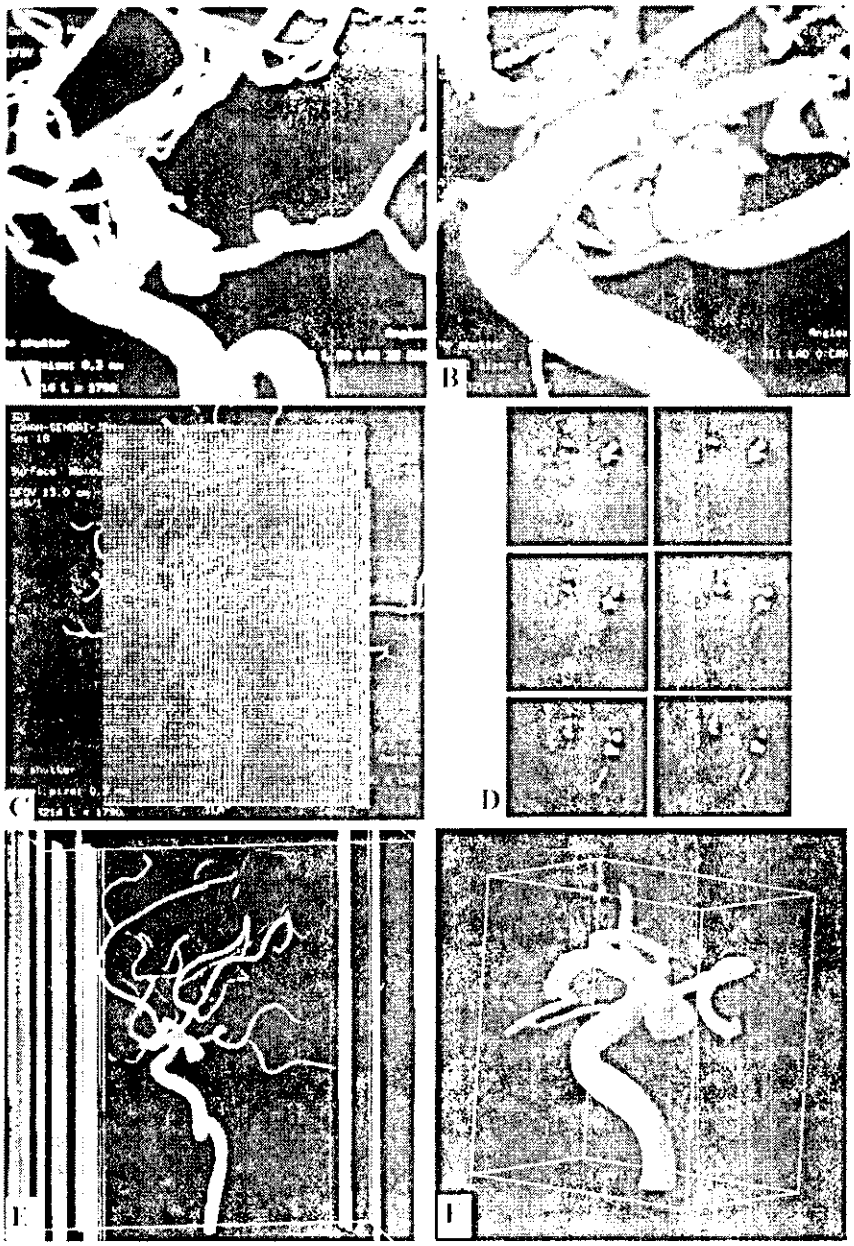

FIG 2. Data transformation from an angiographic image into a computational grid model.

A and *B*, 3D DSA images (different views) of a posterior communicating artery aneurysm.

C, Typical setup for reformatting of the angiographic image into 585 secondary DICOM sections in a 13-cm displayed field of view.

D, Sequential secondary DICOM sections. The respective files are concatenated before processing with DICOM reader (X) MedCon.

E, 3D gray-scale raster image produced by (X) MedCon and imported by AVS/Express. Columns are patient data and image parameters still present in the file.

F, Result of image manipulations with AVS/Express. ROI is cut out and the luminal vascular surface is identified with a gray-scale isosurface value of 1500. This ROI includes the aneurysm and its small branching vessel. (Figure continues.)

sections and a 0.3–1-mm section thickness (equal to 1 voxel). Section sets of less than 300 images were not promising in terms of final computational mesh quality.

MR Angiography

3D time-of-flight (TOF) MR angiography (MRA) was performed by using a 1.5-T MR imaging system (Signa Horizon; GE Medical Systems). A standard head coil was used for imaging of the head (Fig 3A). 3D TOF MRA was performed by using the following imaging parameters: TR/TE, 30/3.2; flip angle, 20°; section thickness, 0.8 mm; slab thickness, 64 mm; matrix, 256 × 256; and field of view, 16 cm.

CT Angiography

CT angiography (CTA) was done by using a helical CT scanner (LightSpeed Plus-U; GE Medical Systems) with multidetector-row capability (where one scan equaled eight sections). The data presented in Figure 3 were obtained by using a section thickness of 1 mm with a 0.63-mm interval between the sections and a table speed of 8.75 mm/s (140 kV, 180 mAs). Zero-degree table and gantry tilt were used. Sections in DICOM format were acquired with a 512 × 512 matrix. Scanning was started at the C1 level and continued cranially parallel to orbitomeatal line to the skull vertex during the intravenous injection of contrast material at a rate of 3 mL/s.

The digital images and the respective files obtained so far could not be directly used for grid generation. The luminal surface of blood vessels was extracted from them in the format suitable for import by grid generators. This was done, for instance, by using the Advanced Visual Systems/Express (AVS/Express Visualization Edition, version 5.1). Step II and tools 2 and 3 of our procedure (Fig 1) were needed to convert our files into a proper format for AVS/Express input.

Merging of Section Files and DICOM Reader Software

First (Fig 1, tool 2), all DICOM files were combined into a single one, a standard operation for any computer operating

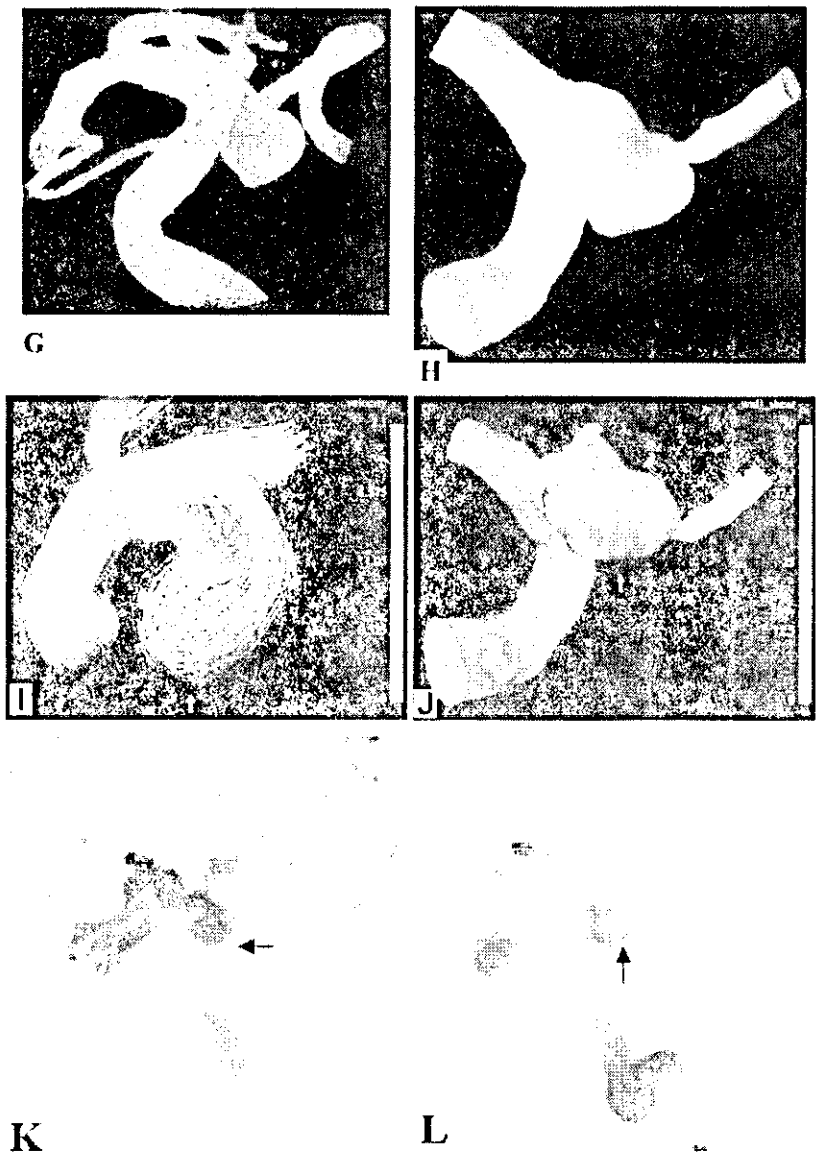

FIG 2. Continued.

G, AVS/Express STL file containing the surface mesh is imported by using the ICEM CFD Mesh Editor and Tetra grid generator. These tools allow us to further remove unnecessary parts, manually repair and smooth the surface mesh, close inflow and outflow boundaries, and generate the volume grid.

H, Final computational tetrahedral grid model for blood flow simulation with Fluent or another suitable software.

I, Typical instant streamlines colored by velocity (in m/s) show that the entering bloodstream hits the aneurysm wall at the angiographically determined rupture area (*arrow*).

J, Typical instant wall shear-stress distribution (Pa) shows a local shear-stress maximum where the aneurysm ruptured (*arrow*).

K, Arterial-phase 2D DSA image shows escape of a linear stream of contrast agent into the subarachnoid space (*arrow*).

L, Arterial-phase 2D DSA image obtained during endovascular intervention shows escape of the coils through the aneurysm rupture (*arrow*).

system (eg, Unix, Windows, Mac OS). In the present work, this was done on a Unix computer with the concatenate command. With Microsoft Windows, the copy command allowed us to perform such file merging.

Second, (Fig 1, tool 3), the resulting single file was imported by using the X-windows medical image conversion utility (X) MedCon (version 0.5.10; Erick Nolf, Ghent University Hospital, Ghent, Belgium). The conversion utility always used original image dimensions and pixel values. This DICOM reader could output files in raw binary or ASCII formats. The binary output format included binary image data with all other information (eg, image size, patient's name) contained in the original section image files. This additional information was to be cut later by using AVS/ Express. The resulting file at this stage contained a 3D raster gray-scale image (Fig 2E). (More details can be found at *http://xmedcon.sourceforge.net*.)

AVS/Express Visual Development Tool

The main role of the AVS/Express visual development tool (AVS, Waltham, MA) (Fig 1) was to define the region of interest (ROI) and to extract the luminal vascular surface from the 3D raster gray-scale image obtained at the previous stage (Fig 2). Detailed information about AVS commands may be obtained at *www.avs.com*.

Using the AVS isosurface command, we could extract the luminal vascular surface, triangulating it and writing into a file in stereolithography (STL) format. It used voxel intensities ranging from 0 to 4000. The procedure was fully automatic and based on picking up the data corresponding to some specified fixed value and connecting the respective points, thus forming surface triangles. In our experience, the specific gray-scale isosurface value corresponding to the luminal vessel surface could be determined by trial and error, aiming at the best appearance of the surface, in a range from 1100 to 1800 for 3D DSA data and in a range of 200–400 for MRA and CTA data. The STL format could be used as geometry input format in most modern commercial grid generators (Figs 2F, 3B, and C).

Measurements of maximum aneurysmal diameters, aneurysmal neck diameters, diameters of parent arteries, and other dimensions were performed on the luminal vascular surfaces in the 3D DSA images and their respective reconstructed meshes. The comparable measurements were statistically analyzed by using multiple regression analysis (StatView, version 5.0.1; SAS Institute, Cary, NC). The error probability values ($P < .0001$) and the estimated standard error (SE = 0.007) were calculated.

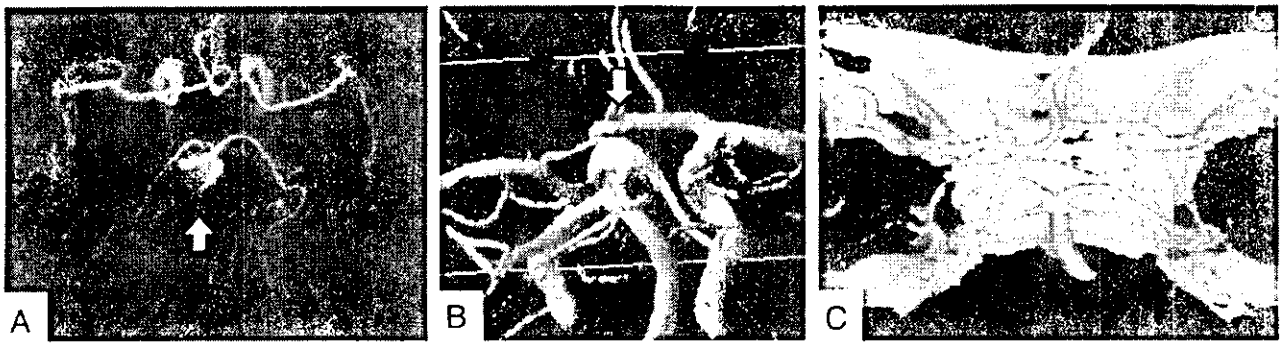

FIG 3. Examples of four vessels reconstructed from MRA image and CTA data.

A, MRA data of four vessels with basilar top aneurysm (arrow).

B, Surface grid reconstruction of MRA image data. Note the inferior quality of this grid, as compared with that obtained from 3D DSA and multiple defects in the vessel walls.

C, Surface grid reconstruction (STL file) from CTA of four vessels of a normal circle of Willis. Note the reconstructed skull base requiring manual removal during mesh generation.

Grid Generator

The next stage (Fig 1, stage IV) was volume grid generation. The grid generation software (ICEM CFD version 4.1; ICEM CFD Engineering) was used to divide our model into tetrahedral cells. (Tetrahedral grids are widely used in CFD for computational models of complex shape.) The Mesh Editor and Tetra tools allowed us to cut additional unnecessary parts not related to our ROI to close the computational domain to define inlets, outlets, and wall boundaries (Fig 2G and H). Interactive modifications of the individual grid node coordinates could be done as well to eliminate unneeded small branches and false vessel connections. Finally, mesh smoothing further improved grid quality. The grid generator also allowed us to construct a triangular, prismatic, layered mesh representing vascular walls of finite thickness. This was needed for coupled flow-dynamic and elastodynamic simulations that took into account the deformations, stresses, and displacements of the vessel walls (Fig 4). (Further details can be found at *www.icemcfd.com*.)

The number of grid nodes or tetrahedrons was chosen as a reasonable compromise between better accuracy and shorter computational time of subsequent simulations. In the ICEM CFD grid generator, a nondimensional parameter Tetra determined the size of tetrahedral mesh units to be generated and, hence, the number of grid nodes, the mesh resolution, and the accuracy of the subsequent calculations. Test computations were performed for the same model with different Tetra values: 1.0, 0.5, and 0.25. It was found that the Tetra value 0.5 was small enough to get a reasonably converged solution (ie, further reduction of the parameter did not lead to considerable changes in the solution) within acceptable computational time. The numbers of nodes and tetrahedrons in the grids used to compute the cases presented in Figures 2 and 5 were within the ranges 26,000–48,000 and 170,000–285,000, respectively. The prismatic-tetrahedral grids in Figure 4 contain 7049 (case I) and 17,060 (case II) nodes.

Computational grids obtained from stages I–IV (Fig 1) could be applied to numerical simulations of blood flow in the respective geometry by using CFD software (Fidap; Fluent Inc., Lebanon, N.H.).

Flow Modeling

The unsteady 3D incompressible Navier-Stokes equations are widely used for blood flow simulations. Blood is usually considered a Newtonian fluid; this is a fairly good approximation for large-bore vessels. Our simulations were performed with the following material constants: blood density, 1060 kg/m^3; and blood dynamic viscosity, 0.004 Poiseuille.

To achieve truly patient-specific modeling, the boundary condition at the inflow boundary was based on the pulsatile periodic flow rate obtained during sonography of intracranial vessels. Because the governing equations and boundary conditions included only the pressure gradient, the simulation produced relative pressure values to be considered with respect to a basal pressure.

The unsteady flows in aneurysms were computed for an interval of 3 seconds (over three cardiac cycles). The results corresponding to the last, third cycle were considered independent of the initial conditions and used for flow analysis. We performed several computations for the same model with different time steps: 0.1 second (30 steps), 0.025 second (120 steps), and 0.01 second (300 steps). As long as the grid-converged solution was obtained (ie, the grid was fine enough), the time step values did not dramatically influence the results at a certain instant of the cardiac cycle (eg, at the systolic peak). The time step of 0.025 second seemed to provide a reasonable compromise in terms of accuracy and computational time and for plotting and statistical analysis.

As to the walls of the vessels, two main possibilities exist. The first and simplest approach was to consider them as rigid structures. The second was to account for their movement and deformation. In the latter, an elastic model was chosen, with its parameters to be determined.

Rigid Vessels

Under this assumption, any CFD code with incompressible fluid-modeling capabilities can be used. We applied Fluent software (version 6.0.12) (Fluent Inc., Lebanon, NH) to compute physiologic pulsating flows. In the code, the governing equations written in strong conservative form for mass and momentum were discretized with a finite-volume method. We chose the SIMPLE method to solve the discretized equations. To improve the convergence speed, relaxation factors were applied to velocity and pressure modifications. (Detailed information about the code is available at *www.fluent.com*.)

On the rigid vessel walls, the nonslip and nonpenetration conditions were applied (ie, all velocity components at the vessel walls were set to zero). For the outlet, the Fluent outflow boundary condition was used. The typical computational time on the grids just mentioned was approximately 8–12 hours on a single processor (Origin 2000; Silicon Graphics Inc).

Deformable Vessels

This model required a fluid-structure interaction approach accounting for both instantaneous fluid forces acting on the walls of vessels and for effects of the walls' motion on the fluid dynamic field. The number of software packages that included fluid-structure interaction capabilities was relatively limited.

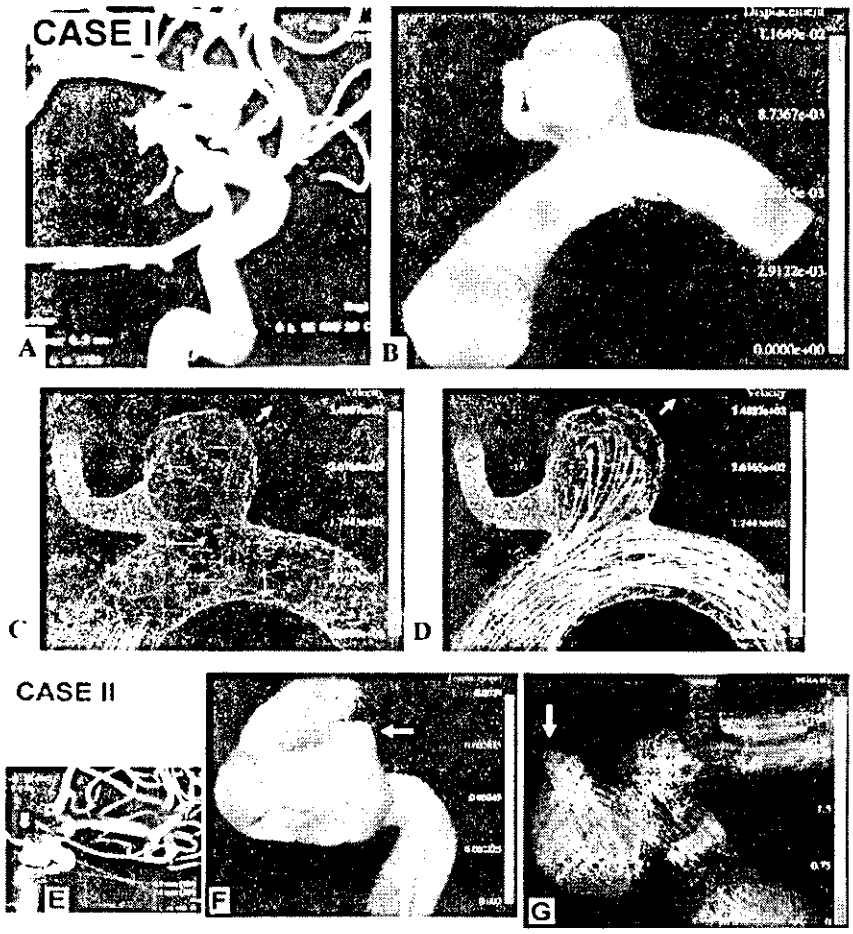

FIG 4. Computations for grid models with moving walls. Case I: *A*, 3D DSA image of a nonruptured internal carotid–posterior communicating aneurysm. *B*, Displacement (in mm) of the aneurysm wall at the systolic peak. *Red* is maximal displacement. *C* and *D*, Movie frames illustrate deformation of the aneurysm from early systole (*C*) to midsystolic peak (*D*). *Arrow* indicates the direction of movement (and possible future growth). Bloodstream enters the aneurysm, hits its wall, decelerates (note change in color; velocity in cm/s), and exerts pressure resulting in maximal displacement. Case II: *E*, 3D DSA image of a nonruptured carotid cave aneurysm. *F*, Displacement of the aneurysm wall at the systolic peak. *Red* is maximal displacement at the nonruptured aneurysmal bleb (*arrow*). *G*, Typical instant streamlines show that the entering bloodstream hits the aneurysm wall at the angiographically determined bleb (*arrow*), exerting pressure that results in maximal displacement.

Fidap (Fluent Inc., Lebanon, NH) code was used to carry out the simulations presented in Figure 4.

In this code, an Arbitrary Lagrangian Eulerian (ALE) algorithm was used. This sought, at each time increment, the convergence of three blocks of equations describing blood dynamics, stresses in vessels' walls, and mesh movements (23). The only Fidap option for vascular walls was a linear elastic homogeneous approximation. The following elastic material constants were used: Young modulus of 2.7 Mpa and Poisson coefficient of 0.45 (18). The cases in Figure 4 took more than 4 days to compute on a single processor (Origin 2000; Silicon Graphics Inc). (A description of Fidap can be found at *www.fluent.com*.)

Flow Visualization

Fluent, Fidap, and other CFD software packages have their own visualization tools that are sufficient in many cases. However, specialized postprocessing software might offer additional useful options. For instance, we used EnSight (version 7.3.0; Computational Engineering International Inc., Apex, NC), which was general-purpose postprocessing software used in engineering and research and available for all major computer platforms. This was used to create computer animations (movies) of unsteady blood flow through aneurysms based on Fluent and Fidap results (Fig 5). (Details can be found at *www.ensight.com*.)

Results

Figure 2 shows data from a patient with ruptured internal carotid–posterior communicating artery aneurysm and illustrates the whole procedure of computational analysis from 3D DSA to CFD results. The ruptured area was depicted by using angiography (Fig 2K and L). Comparison with the simulation results allowed us to conclude that it corresponded to the area facing the bloodstream entering the aneurysm. The aneurysm wall served as an obstacle decelerating the entering stream (diminishing its velocity) and deflecting it along the wall. This was accompanied by a persisting local fluid-induced wall shear-stress maximum in the area hit by the stream; this might have been one of the reasons for aneurysm rupture.

Figure 3 illustrates surface grid extractions from MRA of the circle of Willis and CTA. One image shows multiple defects in the wall of the basilar artery aneurysm that made surface mesh repair and volume grid generation more time- and labor-consuming than they would have been with "clean" 3D DSA images. Nevertheless, there were no fundamental difficulties, and surface grid reconstruction for sparsely sampled MRA-based objects was attainable with the proposed approach. CTA showed promising mesh quality that may be useful for studying flow dynamics of the intracranial vessels. However, manual removal of the reconstructed skull base bone was necessary.

Figure 5 illustrates another attempt at computational diagnosis of the rupture area of MCA aneurysms, with subsequent surgical validation. Similar to

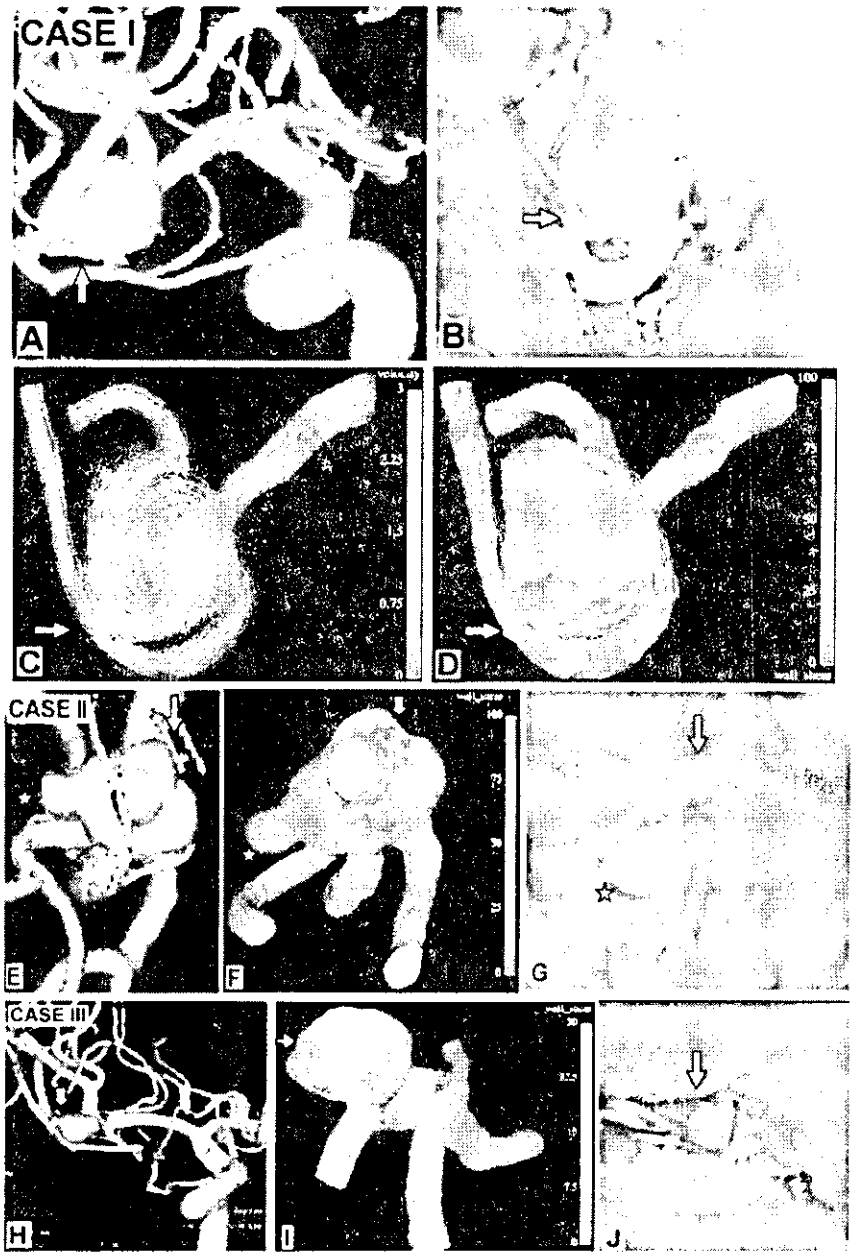

FIG 5. Computational results for grid models with rigid walls compared with operative photos and 3D DSA images. Case I: *A*, 3D DSA shows a ruptured middle cerebral artery (MCA) bifurcation aneurysm. *B*, Operative photo shows the aneurysm and a curved branch coming from it, the lower trunk of the MCA. Note a surgical instrument pointing to the ruptured zone on the aneurysm wall (*arrow*) under the genu of the lower trunk of the MCA. *C*, This zone faces the blood stream entering the aneurysm (*arrow, velocity* in *m/s*). *D*, Wall exposed to high shear stress (*arrow*, units of Pa). Case II: *E*, 3D DSA of a ruptured MCA bifurcation aneurysm with multiple blebs. *F*, Typical instant wall-shear-stress distribution (Pa) shows a local shear-stress maximum where the aneurysm ruptured (*arrow* in *F*). Largest bleb (*star*) in the low-shear-stress area of the aneurysm wall. *G*, At surgery, this was not ruptured and had an intact wall. Dome blebs in the high shear stress area (*arrow*) in front of the coming bloodstream were the ruptured ones and were tentatively clipped (*arrow*). Case III: *H*, 3D DSA image of a small, ruptured MCA bifurcation aneurysm. *I*, Typical instant wall-shear-stress distribution shows a local shear-stress maximum where the aneurysm ruptured (*arrow*). 3D orientations of the aneurysm are similar in *I* and *J*, an operative photo showing the aneurysm in the sylvian fissure after proximal clip placement of the MCA and a thin-walled, ruptured area (*arrow*) where the aneurysm had maximum local shear stress.

a previous case (Fig 2), the ruptured area corresponded to the area where the entering blood stream first hit the wall (at an angle). Again, high wall-shear stress was seen in this area; this might have been the reason for rupture at this location.

Case I in Figure 4 (nonruptured internal carotid–posterior communicating artery aneurysm) represented successful 3D modeling that accounted for vascular movement and deformation by using Fidap. In correspondence with the findings illustrated in Figures 2 and 5, this figure identified the maximum area of displacement as the area hit by the blood jet entering the aneurysm. The aneurysm was likely to grow in this direction. It was also a primary suspect for the location of possible rupture or bleb formation, as shown in case II in the same figure (nonruptured carotid cave aneurysm). These findings confirmed that the maximum area of wall displacement is located at the angiographically determined bleb in the aneurysmal inflow zone.

Discussion

The method for anatomic reconstruction of cerebral vessels in the form of computational replicas should work for a broad spectrum of medical imaging techniques, the availability of which varies from one medical center to another. Replicas were obtained from all currently available modalities of cerebral angiography, such as noninvasive screening MRA and CTA, which can sometimes replace 3D DSA in diagnosing intracranial aneurysms (24, 25) and also the invasive, highest-quality 3D DSA. Therefore, our approach was general: It worked with any 3D image